Nanoscale

COMMUNICATION

View Article Online
View Journal

Cite this: DOI: 10.1039/d5nr05182g

Received 10th December 2025,
Accepted 27th March 2026

DOI: 10.1039/d5nr05182g

rsc.li/nanoscale

Effective reactive reach of plasmonic hot holes through molecular barriers

Julian Michael Heeg,[a] Neda Irannejad Najafabadi,[a] Daniel Velev Latchev,[a] Arthur Andreis,[a] Angeliki Betsista,[a] Dan Li,[b] Mikaela Görlin[b] and Jacinto Sá *[a,c]

The efficiency of plasmon-driven oxidation reactions depends on the ability of plasmon-generated hot holes to reach reactive interfaces. Here, we probe the effective reactive reach of plasmonic hot holes using alkanethiol self-assembled monolayers of varying chain length on Au nanoparticles. Operando photocurrent measurements combined with selective bromide poisoning isolate the contribution of hot holes traversing the molecular layer. The resulting activity exhibits a volcano-type dependence on chain length, with maximum reactivity observed for octanethiol (C_8), corresponding to an effective barrier thickness of ~1 nm. Shorter chains enable rapid charge transfer but increase recombination losses, whereas longer chains hinder hole transport across the molecular layer. These findings demonstrate that plasmon-generated hot holes remain chemically reactive across nanometer-scale molecular barriers, with optimal performance achieved when transport occurs within the tunnelling regime.

Hot carriers generated during the non-radiative decay of the light-induced localized surface plasmons in metallic nanoparticles have attracted strong interest for driving photocatalytic redox reactions.[1,2] In particular, *hot holes* play a crucial role in oxidation reactions of organic molecules such as alcohols, which are key steps in solar fuels[3–6] and synthetic and pharmaceutical chemistry.[7,8] Unlike traditional harsh oxidants, plasmon-mediated hot hole oxidation can be initiated under mild conditions with visible or near-infrared light.[9,10]

The efficiency of hot hole-driven transformations depends strongly on their generation, transport, and lifetime within the nanoparticle and across interfaces.[11–13] Gold nanoparticles (Au NPs) are especially promising due to their tunable localized surface plasmon resonance (LSPR) in the visible range[6] and their stability as oxidation catalysts.[14] While the extraction of hot electrons across Schottky junctions has been widely explored,[15–17] direct measurement of hot hole transport and their effective range remains challenging.[18]

Chidsey's pioneering work on electron tunnelling through alkanethiols,[19] inspired approaches to probe plasmonic hot electron transport lengths on Au NPs surfaces functionalized with self-assembled monolayers (SAMs) of thiols. By systematically varying the chain length, these studies established effective distances and efficiencies of hot electron transfer.[20] Building on this concept, we hypothesize that a similar strategy can be employed to probe how molecular barrier thickness governs plasmonic hot-hole-mediated interfacial reactivity.

In this study, we investigated the effective reactive reach of plasmon-generated hot holes across molecular barriers within thiol-functionalized Au nanoparticles and their role to drive interfacial chemistry reactions. By applying chronoamperometry under controlled plasmonic excitation, we correlated the structure of the thiol SAMs with the resulting photocurrent, allowing us to identify an effective molecular barrier thickness at which hot-hole-mediated oxidation is maximized (Fig. 1). This provides fundamental insight into charge separation and migration in plasmonic systems and establishes essential design guidelines for optimizing plasmon-assisted catalysis.

The plasmonic electrode employed in this work operates on an energy-selection strategy adapted from our previously established designs,[21,22] in which a dielectric barrier is utilized to control the extraction of photoexcited charge carriers. When metal nanoparticles absorb visible light, plasmon dephasing generates electrons and holes spanning a wide energy range. By introducing an interfacial layer with a well-defined band alignment, only carriers possessing sufficient excess energy can cross into the underlying collector, effectively imposing a threshold on charge transfer. This selective gating separates high-energy carriers from the thermal background and enables controlled access to the energetic fraction responsible for driving redox chemistry.

Fabrication of the plasmonic electrode followed established procedures, with full details provided in the SI. Briefly, a 10 nm amorphous TiO_2 layer was deposited on FTO *via* chemi-

[a]*Department of Chemistry-Ångström, Division of Physical Chemistry, Uppsala University, Box 520, 751 21 Uppsala, Sweden. E-mail: jacinto.sa@kemi.uu.se*
[b]*Department of Chemistry-Ångström Laboratory, Division of Structural Chemistry, Uppsala University, Box 538, 751 21 Uppsala, Sweden*
[c]*Institute of Physical Chemistry, Polish Academy of Sciences, Marcina Kasprzaka 44/52, 01-224 Warsaw, Poland*

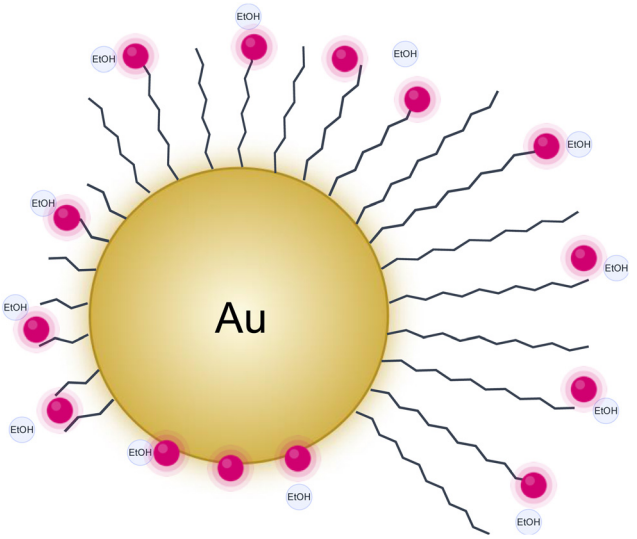

Fig. 1 Schematic illustration of the experimental concept used to test the hole transfer length hypothesis on Au NPs surfaces functionalized with self-assembled monolayers (SAMs) of thiols.

cal vapor deposition by NSG-Pilkington to serve as a pinhole-free energy filter that electronically decouples the Au nanoparticles from the collector and selectively extracts electrons with excess energies above ~0.5–0.6 eV, while blocking lower-energy electrons and hot holes. The energetic filtering behaviour of this TiO_2 layer has been previously introduced and experimentally validated for an essentially identical FTO/TiO_2/Au nanoparticle architecture, and the same TiO_2 thickness, deposition method, and electrode configuration are employed in the present study.[21]

A thin 2 nm Au film was deposited *via* physical vapor deposition onto the FTO/TiO_2 substrate and subsequently annealed in air at 723 K for 30 min to produce a dense array of 10–14 nm gold nanoparticles (Au NPs) (Fig. 2), which exhibited a localized surface plasmon resonance near 594 nm (Fig. 3). Note that the optical trace represents the net absorbance, obtained by subtracting the FTO/TiO_2 substrate spectrum from the measured signal.

Introducing a SAM layer onto the electrode did not cause a measurable change in the Au LSPR absorbance (see representative example in Fig. 3). This indicates that the SAM does not alter the optical properties of the plasmonic nanoparticles to an extent that could influence their response. Consequently, the activity changes discussed below cannot be ascribed to optical phenomena, but rather to modifications in charge transfer or interfacial processes.

Catalytic activity towards ethanol oxidation was evaluated through photocurrent measurements in a three-electrode electrochemical setup (see SI for more detail). The plasmonic substrate served as the working electrode, a Pt wire was used as the counter electrode, and a non-aqueous Ag/Ag^+ electrode acted as the reference electrode. A continuous-wave 635 nm laser (maximum intensity: 132 mW cm^{-2}) illuminated a

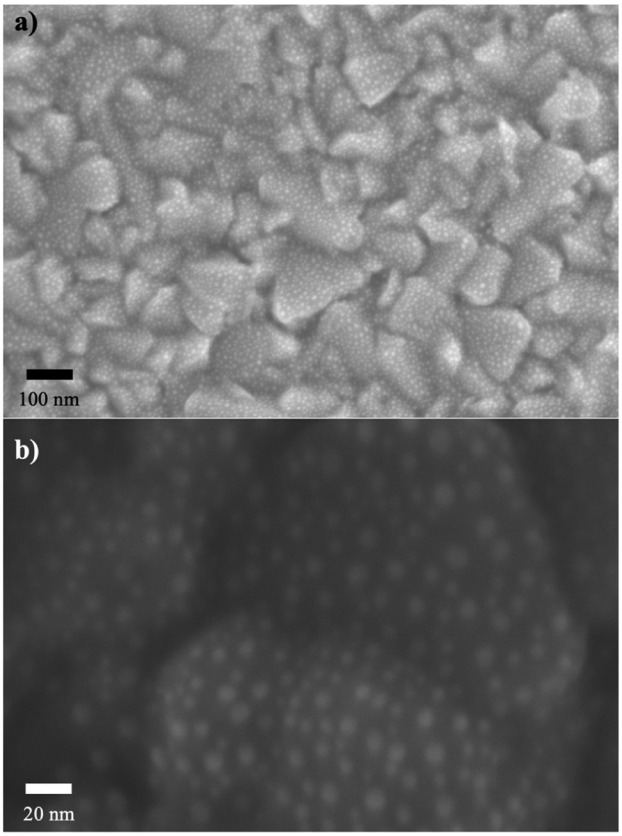

Fig. 2 Scanning electron microscopy (SEM) images of Au NPs deposited on an FTO/TiO_2 substrate, collected at an acceleration voltage of 5.00 kV. (a) Low-magnification image (200×); (b) high-magnification image (1000×).

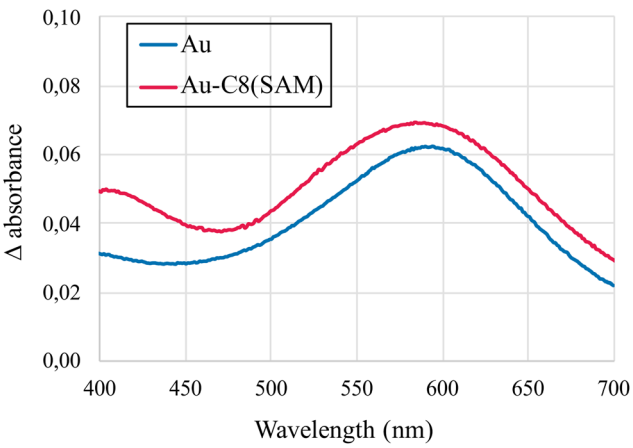

Fig. 3 Net visible absorbance of Au NPs on an FTO/TiO_2 substrate, and the effect of introducing a SAM layer.

0.95 cm^2 area of the working electrode, and the beam was modulated at 0.5 Hz. This modulation frequency was chosen because it allows clear separation of photocatalytic contributions from heat-driven responses, which can otherwise complicate plasmonic measurements.[21]

To assess whether thermal effects contribute to the measured photocurrent, the temperature of both the electrolyte and the electrode surface was monitored using a thermocouple during illumination. The observed temperature changes were consistent with uniform laser heating of the system and did not indicate plasmon-induced photothermal contributions. Accordingly, bare FTO/TiO_2 substrates were used as controls to establish a baseline response. Under identical illumination, bias, and modulation conditions, no measurable photocurrent was detected, demonstrating that the temperature increase alone is insufficient to drive ethanol oxidation. Consistently, FTO/TiO_2 electrodes exposed to alkanethiol and NaBr also showed no photocurrent, as expected given the low applied bias and the non-photoactive nature of amorphous TiO_2 under 635 nm illumination.

It is worth noting that, according to X-ray photoelectron spectroscopy (XPS) survey analysis, the alkanethiol content estimated from the S 2p signal and the NaBr content estimated from the Br 3d signal – both normalized to the Ti 2p signal – were consistently below 3% for S and 6% for Br. These values are significantly lower than those obtained in the presence of Au NPs (discussed below), which is consistent with the preferential attachment of alkanethiols and Br^- to Au.

The stepwise, *in situ* surface functionalization of the same plasmonic electrodes rules out variations in Au nanoparticle loading or distribution as the source of the observed changes in photocatalytic activity, indicating that they stem from the introduced interfacial modifications. In the present study, the alkanethiol monolayers are used as a controlled molecular barrier family rather than as idealized, defect-free tunnelling spacers, and the observed trends reflect effective barrier properties under identical assembly conditions.

To further assess whether the surface coverage of alkanethiol monolayers varies significantly with ligand chain length, additional electrochemical impedance spectroscopy (EIS) measurements were performed on SAM modified electrodes. In the standard electrode architecture, a TiO_2 insulating layer is placed between the Au NP light absorber and the conductive FTO substrate to act as an energy filter. While this configuration is advantageous for device operation, it complicates reliable EIS measurements. To address this limitation, additional electrodes were prepared with a much thinner TiO_2 layer (*ca.* 5 nm). SEM analysis confirmed that the resulting FTO/Au NP electrodes exhibit Au nanoparticles with an average diameter of 7–8 nm, with a minor population of larger particles (~20 nm) representing less than 5% of the particles observed. Although the average particle size is slightly smaller than in the standard electrodes, the exposed Au surface remains comparable and therefore suitable for evaluating SAM formation.

The EIS spectra display two characteristic semicircles (Fig. S6): a smaller semicircle associated with the counter electrode and a larger semicircle corresponding to the electrode/electrolyte interface. Bare Au NP electrode exhibits a smaller interfacial resistance compared with thiol-functionalized electrodes, consistent with the presence of surface-bound ligands. However, the differences between electrodes functionalized with alkanethiols of different chain lengths are relatively minor. A similar trend is observed after treatment with NaBr (Fig. S6): although the overall resistance increases, no significant differences between the various thiol-modified electrodes are detected. These observations indicate that the different alkanethiols provide comparable surface coverage of the Au nanoparticles and that NaBr treatment does not significantly alter their relative coverage. This supports the hypothesis that the thiol surface concentration is largely independent of chain length, and therefore the trends observed in the photocatalytic response can be attributed primarily to differences in the effective hole reactive reach rather than variations in SAM surface coverage.

The photocurrent response under pulsed illumination is shown in Fig. 4. Upon switching the light on, a brief anodic spike is observed, corresponding to charging of the electro-

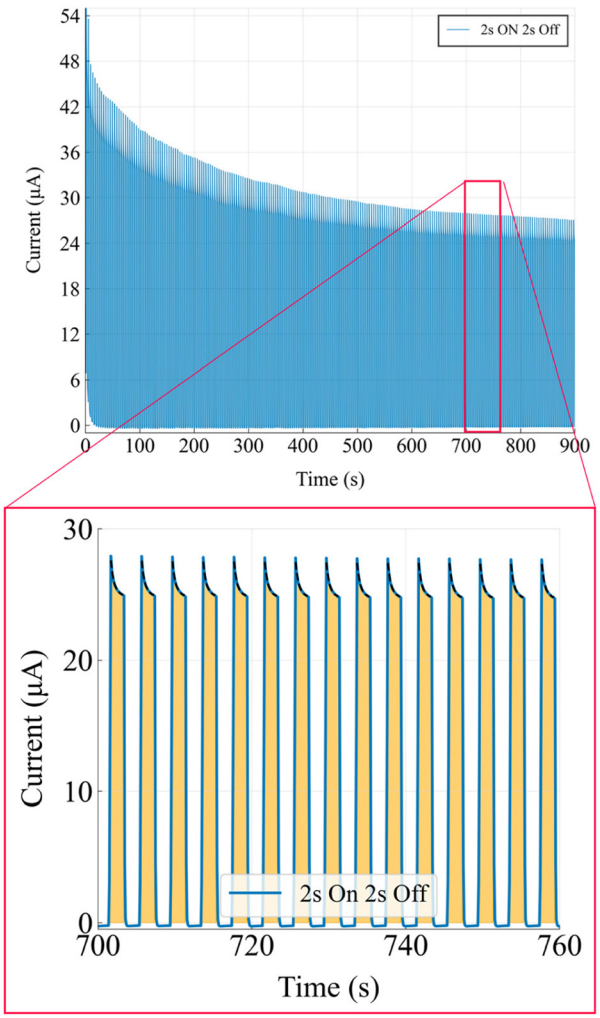

Fig. 4 Photocurrent response of Au NPs supported on an FTO/TiO_2 substrate during ethanol oxidation in 1.6 mM KNO_3/ethanol serving as electrolyte. The lower panel shows an expanded view of the traces, highlighting the stable signal and the square-wave response to light modulation.

chemical double layer and its rapid relaxation. This transient behaviour closely resembles the current–time response reported in classical potential-step studies by Chidsey.[19] As the system approaches steady state, the photocurrent adopts an ideal square-wave profile that follows the light modulation, indicating that the signal arises from a sustained photo-induced interfacial electron-transfer process rather than from heat-driven effects, which typically give rise to slower, cumulative current drifts under continuous illumination.[23,24]

To quantify hot-hole transfer kinetics during photoelectrocatalysis, we applied a modified version of the Chidsey model[19] previously adapted for light-triggered systems, which enables extraction of rate constants from the decay of the photocurrent following each illumination step.[21] To exclude mass-transport limitations, a Cottrell analysis for planar electrodes was applied to each individual light-on transient to identify the onset of diffusion-limited behaviour. Only the data preceding this onset were retained, and charge-transfer rate constants were extracted exclusively from this diffusion-independent time window using the adapted Chidsey approach. Although the electrode consists of nanostructured Au particles, the early-time transient regime analysed here is well described by a planar-electrode approximation, as the fitting is restricted to short times prior to the onset of diffusion-limited behaviour. The complete data-processing workflow is illustrated schematically in Fig. S1 of the SI and exemplified for the data shown in Fig. 4.

The kinetic analysis is based on the potential-step methodology introduced by Chidsey,[19] in which interfacial charge-transfer rate constants are obtained from the temporal decay of the current following a step perturbation. In this framework, the initial transient is associated with charging of the electrochemical double layer, followed by an exponential decay governed by the sum of the forward and backward electron-transfer rates. When diffusion and capacitive contributions are excluded, the decay rate directly reflects the intrinsic interfacial charge-transfer kinetics. In systems incorporating molecular spacers, this approach provides a robust means of probing distance-dependent tunnelling-mediated charge transfer.

After the photocurrent response reached a stable regime, at least 100 illumination cycles (2 s ON, 2 s OFF per cycle) were analyzed to determine average hole-transfer rate constants. For each experimental condition (pristine, SAM-modified, and bromide-poisoned), measurements were performed on multiple independently prepared electrodes ($n \geq 3$). The electrode-to-electrode variability was small compared to the systematic trends observed as a function of alkanethiol chain length, and does not affect the conclusions drawn from the kinetic analysis.

The illumination pulse duration was optimized to reproduce the characteristic current–time response of potential-step experiments described by Chidsey,[19] consisting of a brief anodic transient at light-on followed by a cathodic transient at light-off. Under these conditions, the photocurrent adopts an ideal square-wave profile when the full reaction mixture is present, indicating that the signal arises from non-thermal interfacial charge transfer. Longer illumination periods were found to introduce gradual current evolution associated with photothermal mass-transport effects, whereas shorter pulses suppress these contributions while preserving kinetic information.[23,24] The resulting values are summarized in Table 1. For unmodified (pristine) electrodes, the extracted rates fall within the range of 0.16–0.28 s^{-1}, confirming comparable catalytic quality across the electrodes used in this study.

The SAM layers were formed *in situ* on each electrode following the procedure described in the SI. Electrochemical impedance spectroscopy (EIS) could not be applied to this system because the Au NPs are electronically decoupled from the FTO collector by the insulating amorphous TiO_2 layer, which prevents a measurable response to the small potential perturbations required for EIS. Instead, XPS provides spectroscopic evidence for alkanethiol binding to the Au nanoparticles. Upon functionalization, the S 2p signal increases from <3% (relative to Ti 2p) for FTO/TiO_2 substrates to approximately 7% in the presence of Au nanoparticles, with the S $2p_{3/2}$ component centred at ~162.5 eV, consistent with Au–S bonding.[25] Additional support for partial surface coverage is obtained from bromide poisoning experiments: the Br 3d signal decreases from ~14% on pristine Au NPs electrodes to ~8.3% after alkanethiol functionalization, indicating that a substantial fraction of Au surface sites (*ca.* 40%) is occupied by the SAM. To ensure meaningful comparison across samples, the sulphur content was controlled such that variations among alkanethiol-modified electrodes did not exceed ±10%. Moreover, the absence of photocurrent degradation during repeated illumination cycles confirms the stability of the SAM layers under the applied photoelectrochemical conditions.

In all cases, introduction of the alkanethiol layer resulted in a pronounced decrease in photocurrent (Fig. 5). This suppression is attributed to the increased hole-transfer distance imposed by the molecular layer rather than to a change in the reaction mechanism, as the extracted reaction rate constants remain essentially unchanged (Table 1). The selected alkanethiol chain lengths were chosen to balance statistically resolvable changes in molecular barrier thickness with SAM stability and signal detectability under operando conditions. SEM imaging revealed no detectable changes in nanoparticle morphology or distribution upon alkanethiol functionalization,

Table 1 Estimated ethanol photooxidation rate constants obtained from the adapted Chidsey model. The various thiols used were 1-butanethiol (C_4), 1-octanethiol (C_8), 1-dodecanethiol (C_{12}), and 1-hexadecanethiol (C_{16}), without and with additions of 1 mM NaBr to the 1.6 mM KNO_3/ethanol electrolyte for poisoning effect

Thiol used	Au pristine (s^{-1})	Au-SAM (s^{-1})	Au-SAM + NaBr (s^{-1})
C_4	0.178 ± 0.001	0.408 ± 0.001	0.263 ± 0.003
C_8	0.163 ± 0.001	0.203 ± 0.001	0.309 ± 0.010
C_{12}	0.284 ± 0.001	0.218 ± 0.002	0.367 ± 0.023
C_{16}	0.259 ± 0.001	0.221 ± 0.002	0.266 ± 0.008

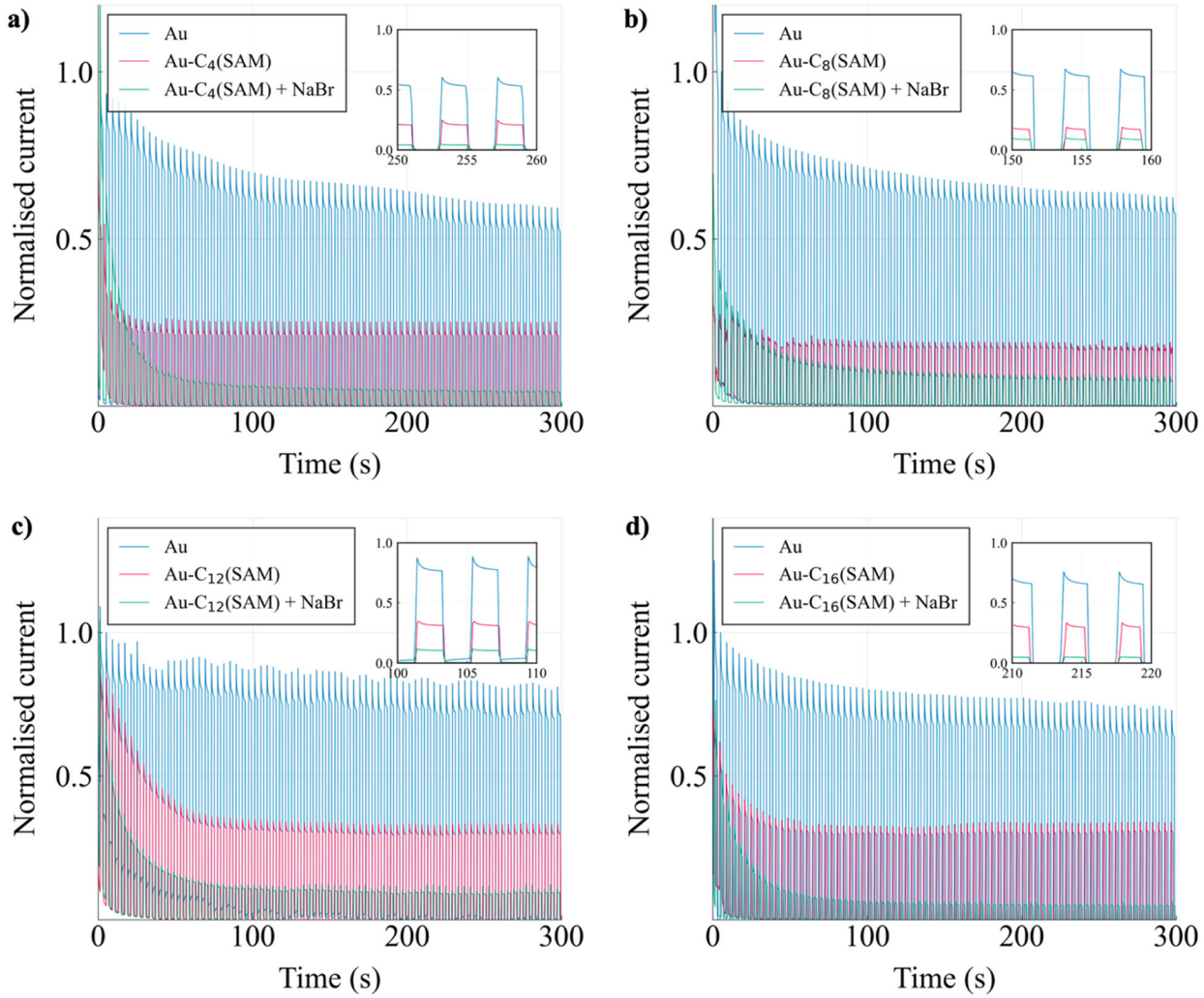

Fig. 5 Overlaid photocurrent traces of pristine Au NPs (blue curves), subsequently functionalized *in situ* with (a) 1-butanethiol (C_4), (b) 1-octanethiol (C_8), (c) 1-dodecanethiol (C_{12}), and (d) 1-hexadecanethiol (C_{16}) (pink curves), and finally poisoned with 1 mM NaBr additives corresponding to the photocurrent dominated by hot-hole reactions (green curves).

consistent with the molecular-scale nature of the SAM modification.

To isolate the dominant photocurrent contribution arising from the SAM-covered Au sites, the SAM-modified electrodes were poisoned by additions of NaBr to the electrolyte consisting of 1.6 mM KNO_3 dissolved in ethanol. Bromide ions selectively adsorb on exposed Au atoms, effectively blocking catalysis at any unfunctionalized surface regions.[26,27] To verify this poisoning effect, we monitored the photocurrent of an unmodified Au electrode after introducing 1 mM NaBr into the electrolyte. As shown in Fig. S2, the photocurrent decays to nearly zero within 100 s on pristine Au + NaBr, confirming that Br^- efficiently suppresses photocatalytic activity originating from bare Au sites. Importantly, no recovery or drift in photocurrent is observed during extended illumination and repeated light modulation, and post-mortem XPS analysis reveals nearly identical Br 3d signal intensities before and after the experiments, indicating that bromide adsorption remains stable throughout the measurements.

XPS of the electrodes before and after NaBr treatment confirms that photocurrent suppression is caused by Br^- adsorption. Following the poisoning step, distinct Br 3d features emerge in the spectrum (Fig. S3), and the Au 4f peak shifts by 0.1 eV to lower binding energy (Fig. S4), indicating electron donation from Br^- to Au^0. These changes are consistent with electronic coupling between the adsorbed bromide ions and the gold surface. These features are absent in the unmodified sample. Importantly, the photocatalytic changes observed upon NaBr addition cannot be ascribed to modifications in the optical response of the Au NPs. The Au LSPR variations are negligible at the excitation wavelength (Fig. S5), ruling out an optical origin for the observed photocurrent decline.

With the suppression of the photocurrent generated by uncovered surface Au atoms through NaBr poisoning, the

remaining signal is dominated by contributions from hot holes that traverse SAM-covered regions of the Au surface under selective site blocking. This enables evaluation of how alkanethiol chain length influences the dominant hot-hole-mediated photocurrent contribution. The resulting data are shown in Fig. 5. The extracted rate constants closely match those obtained previously (Table 1), indicating that the ethanol oxidation mechanism remains unchanged. However, Fig. 5 clearly shows that the photocurrent dominated by hot-hole reactions has a strong dependence with alkanethiol length.

To quantify this trend, the steady-state currents and their averages for each alkanethiol are presented in Fig. 6. For each experiment, the photocurrent measured after alkanethiol functionalization and NaBr poisoning was normalized to the average maximum photocurrent of the corresponding pristine Au nanoparticle electrode recorded under identical illumination and bias conditions. To ensure electrode comparability, only electrodes for which the pristine Au photocurrent varied by less than ±5% were included in the analysis, while electrodes outside this range were excluded.

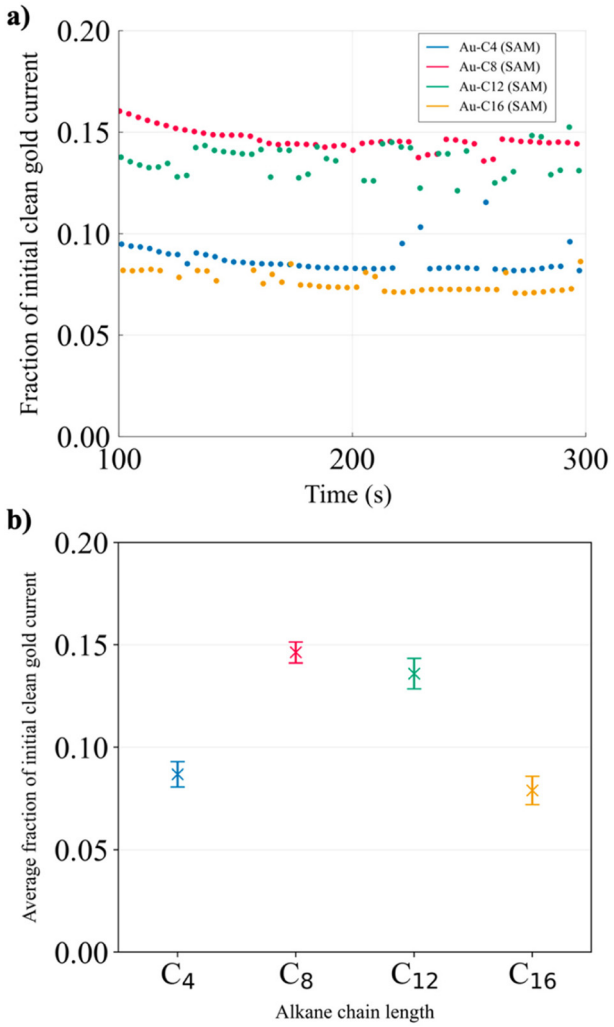

Fig. 6 Photocurrent response associated with ethanol oxidation by hot holes traveling through the SAM layer after addition of 1 mM NaBr. (a) Temporal evolution of the steady-state photocurrent; and (b) average photocurrent as a function of alkanethiol chain length.

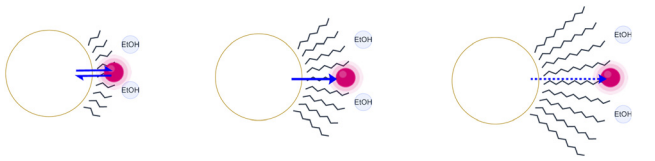

Scheme 1 Illustration of the underlying processes governing ethanol photooxidation as a function of SAM alkanethiol chain length.

The data reveal a volcano-type dependence, with the maximum activity observed for octanethiol (C_8), corresponding to an effective molecular barrier thickness on the order of 1 nm.[28] This behavior can be rationalized using the mechanism illustrated in Scheme 1. For short-chain alkanethiols, hot holes can rapidly reach the substrate surface and react; however, their proximity to the Au nanoparticles increases the likelihood of charge recombination, which limits the catalytic activity relative to the optimum. In contrast, for long-chain alkanethiols (>1 nm), hole transport across the SAM becomes hindered, restricting their ability to reach the reaction interface and thereby reducing the photocatalytic response. Thus, an intermediate chain length (~1 nm) provides the optimal balance: hole transfer is sufficiently fast to compete with recombination while still enabling efficient charge separation.

Taken together, these findings indicate that plasmonic hot holes can remain chemically reactive across nanometer-scale molecular barriers, but maximum reactivity is achieved only when the transport length remains within the tunneling regime, as reported for electrons.[29–31] While recombination and distance-dependent tunnelling provide a physically intuitive framework for interpreting this behaviour, the observed volcano-type dependence should be regarded as an empirical optimum resulting from the interplay of multiple interfacial factors rather than as evidence for a single, uniquely identified mechanism.

Conclusions

This work provides experimental evidence for the molecular-barrier-dependent reactivity of plasmonic hot holes during ethanol photooxidation on thiol-functionalized Au nanoparticles. By combining *in situ* formation of self-assembled monolayers with selective bromide poisoning and operando photocurrent analysis, we isolate the dominant contribution of hot holes that reach catalytic sites through the molecular layer under controlled site blocking. The resulting activity exhibits a volcano-type dependence on alkanethiol chain length, with maximum reactivity observed for octanethiol (C_8), corresponding to an effective molecular barrier thickness of approximately 1 nm. Shorter chains enable rapid interfacial charge

transfer but increase the probability of recombination at the nanoparticle surface, whereas longer chains increasingly hinder hole transport across the molecular layer, limiting overall reactivity.

These findings indicate that plasmon-generated hot holes can remain chemically reactive across nanometer-scale molecular barriers, while optimal catalytic performance is achieved when charge transport remains within the tunnelling regime, consistent with theoretical expectations and prior studies of distance-dependent charge transfer.

The present conclusions are drawn for Au NPs with a narrow size distribution (≈10–14 nm), selected to ensure uniform plasmonic response and high electrode-to-electrode reproducibility. Because hot-carrier energy distributions depend on nanoparticle size, variations in particle diameter are expected to influence hot-hole energetics and may shift the optimal barrier thickness. A systematic exploration of size effects, as well as extension of this approach to other molecular architectures and reactions, represents an important direction for future investigations into plasmon-assisted charge-transfer processes.

Author contributions

J. M. H.: writing – review & editing, conceptualization, experimentation, data analysis and representation. D. V. L.: writing – review & editing, experimentation. A. A.: writing – review & editing, experimentation. M. G.: writing – review & editing, experimentation. J. S: writing – original draft, supervision, financing and conceptualization.

Conflicts of interest

There are no conflicts to declare.

Data availability

All data in the main text or the supplementary information (SI) are available upon request.

Supplementary information is available. See DOI: https://doi.org/10.1039/d5nr05182g.

Acknowledgements

The authors gratefully acknowledge financial support from the Knut and Alice Wallenberg Foundation (grant 2019-0071) and Olle Engkvist Foundation (233-0308). Editorial assistance was provided through language editing services and AI-assisted tools, including OpenAI's ChatGPT, which was used to improve grammar and clarity during manuscript preparation. M. G. acknowledges financial support from the Åforsk foundation (grant 21-384) and STandUP for Energy.

References

1 M. L. Brongersma, N. J. Halas and P. Nordlander, *Nat. Nanotechnol.*, 2015, **10**, 25–34.
2 A. Wach, R. Bericat-Vadell, C. Bacellar, C. Cirelli, P. J. M. Johnson, R. G. Castillo, V. R. Silveira, P. Broqvist, J. Kullgren, A. Maximenko, T. Sobol, E. Partyka-Jankowska, P. Nordlander, N. J. Halas, J. Szlachetko and J. Sá, *Nat. Commun.*, 2025, **16**, 2274.
3 Y. Kim, J. G. Smith and P. K. Jain, *Nat. Chem.*, 2018, **10**, 763–769.
4 S. Mubeen, J. Lee, N. Singh, S. Krämer, G. D. Stucky and M. Moskovits, *Nat. Nanotechnol.*, 2013, **8**, 247–251.
5 S. Linic, P. Christopher and D. B. Ingram, *Nat. Mater.*, 2011, **10**, 911–921.
6 U. Aslam, V. G. Rao, S. Chavez and S. Linic, *Nat. Catal.*, 2018, **1**, 656–665.
7 H. G. Yayla, H. Wang, K. T. Tarantino, H. S. Orbe and R. R. Knowles, *J. Am. Chem. Soc.*, 2016, **138**, 10794–10797.
8 R. Bericat-Vadell, P. Sekar, Y. Patehebieke, X. Zou, N. Kaul, P. Broqvist, R. Lindblad, A. Lindblad, A. Arkhypchuk, C.-J. Walletin and J. Sá, *Mater. Today Chem.*, 2023, **34**, 101783.
9 H. Chalabi and M. L. Brongersma, *Nano Lett.*, 2014, **14**, 1374–1380.
10 S. Linic, U. Aslam, C. Boerigter and M. Morabito, *Nat. Mater.*, 2015, **14**, 567–576.
11 A. Manjavacas, J. G. Liu, V. Kulkarni and P. Nordlander, *ACS Nano*, 2014, **8**, 7630–7638.
12 C. Clavero, *Nat. Photonics*, 2014, **8**, 95–103.
13 L. V. Besteiro, X. Yu and A. O. Govorov, *ACS Photonics*, 2015, **2**, 1231–1238.
14 B. Hammer and J. K. Norskov, *Nature*, 1995, **376**, 238–240.
15 Y. Tian and T. Tatsuma, *J. Am. Chem. Soc.*, 2005, **127**, 7632–7637.
16 A. Furube, L. Du, K. Hara, R. Katoh and M. Tachiya, *J. Am. Chem. Soc.*, 2007, **129**, 14852–14853.
17 T. Tatsuma, H. Nishi and T. Ishida, *Chem. Sci.*, 2017, **8**, 3325–3337.
18 G. Tagliabue, J. S. DuChene, M. Abdellah, A. Habib, D. J. Gosztola, Y. Hattori, W.-H. Cheng, K. Zheng, S. E. Canton, R. Sundararaman, J. Sá and H. A. Atwater, *Nat. Mater.*, 2020, **19**, 1312–1318.
19 C. E. D. Chidsey, *Science*, 1991, **251**, 919–922.
20 F. P. García de Arquer, A. Mihi and G. Konstantatos, *Nanoscale*, 2015, **7**, 2281–2288.
21 P. Sekar, R. Bericat-Vadell, Y. Patehebieke, P. Bröqvist, C.-J. Wallentin, M. Görlin and J. Sá, *Nano Lett.*, 2024, **24**, 8619–8625.
22 R. Bericat-Vadell and J. Sá, *Small Struct.*, 2025, 2500185.
23 M. Maley, J. W. Hill, P. Saha, J. D. Walmsley and C. M. Hill, *J. Phys. Chem. C*, 2019, **123**, 12390–12399.
24 A. J. Bagnall, S. Ganguli and A. Sekretareva, *Angew. Chem., Int. Ed.*, 2024, **63**, e202314352.

25 H.-L. Zhang, S. D. Evans, J. R. Henderson, R. E. Miles and T. Shen, *J. Phys. Chem. B*, 2003, **107**, 6087–6095.
26 B. D. Chandler, S. Kendell, H. Doan, R. Korkosz, L. G. Grabow and C. J. Pursell, *ACS Catal.*, 2012, **2**, 684–694.
27 S. M. Oxford, J. D. Henao, J. H. Yang, M. C. Kung and H. H. Kung, *Appl. Catal., A*, 2008, **229**, 180–186.
28 S. G. Wang, T.-W. Kim, T. Lee, W. Wang and M. A. Reed, *Comprehensive Nanoscience and Technology*, Elsevier Inc., 2011, pp. 463–487. DOI: 10.1016/B978-0-12-374396-1.00138-0.
29 D. J. Wold, R. Haag, M. A. Rampi and C. D. Frisbie, *J. Phys. Chem. B*, 2002, **106**, 2183–2186.
30 W. Wang, T. Lee and M. A. Reed, *J. Phys. Chem. B*, 2004, **108**, 18398–18407.
31 E. Adaligil and K. Slowinski, *J. Electroanal. Chem.*, 2010, **649**, 142–148.